

## RESEARCH ARTICLE

## Thermal stability of ice on Ceres with rough topography

10.1002/2015JE004887

## Key Points:

- Water ice is stable over 10,000 square kilometers on Ceres' surface for billion-year timescales
- Cohesive blocks of ice may have lifetimes of > 10,000 years at low latitudes on Ceres
- Seasonal sublimation of ground ice could explain water vapor observed at Ceres

## Correspondence to:

P. O. Hayne,  
Paul.O.Hayne@jpl.nasa.gov

## Citation:

Hayne, P. O., and O. Aharonson (2015), Thermal stability of ice on Ceres with rough topography, *J. Geophys. Res. Planets*, *120*, 1567–1584, doi:10.1002/2015JE004887.

Received 6 JUL 2015

Accepted 21 AUG 2015

Accepted article online 26 AUG 2015

Published online 29 SEP 2015

P. O. Hayne<sup>1,2</sup> and O. Aharonson<sup>2,3</sup>

<sup>1</sup>Jet Propulsion Laboratory, California Institute of Technology, Pasadena, California, USA, <sup>2</sup>Division of Geological and Planetary Sciences, California Institute of Technology, Pasadena, California, USA, <sup>3</sup>Helen Kimmel Center for Planetary Science, Weizmann Institute of Science, Rehovot, Israel

**Abstract** The dwarf planet Ceres may have an ice-rich crust, and subsurface ice exposed by impacts or endogenic activity would be subject to sublimation. We model surface and subsurface temperatures on Ceres to assess lifetimes of water ice and other volatiles. Topographic shadowing allows a small but nonnegligible fraction (~0.4%) of Ceres' surface to be perennially below the ~110 K criterion for 1 Gyr of stability. These areas are found above 60° latitude. Other molecules (CH<sub>3</sub>OH, NH<sub>3</sub>, SO<sub>2</sub>, and CO<sub>2</sub>) may be cold trapped in smaller abundances. A model for the transport, gravitational escape, and photoionization of H<sub>2</sub>O molecules suggests net accumulation in the cold traps. Buried ice is stable within a meter for > 1 Gyr at latitudes higher than ~50°. An illuminated polar cap of water ice would be stable within a few degrees of the poles only if it maintained a high albedo (>0.5) at present obliquity. If the obliquity exceeded 5° in the geologically recent past, then a putative polar cap would have been erased. At latitudes 0°–30°, ice is stable under solar illumination only briefly (~10–100 years), unless it has high albedo and thermal inertia, in which case lifetimes of > 10<sup>4</sup> years are possible. Finally, a small hemispheric asymmetry exists due to the timing of Ceres' perihelion passage, which would lead to a detectable enhancement of ice in the northern hemisphere if the orbital elements vary slowly relative to the ice accumulation rate. Our model results are potentially testable during the Dawn science mission.

## 1. Introduction

Temperature is the fundamental quantity controlling the stability of condensed volatiles on planetary surfaces. Diurnal, seasonal, and interannual variations in temperature can drive volatiles to cold traps, which may be located at other (typically polar) geographic locations or beneath the surface [Schorghofer, 2007; Schorghofer and Taylor, 2007; Paige et al., 2010]. If temperatures remain low enough, ice deposits may resist sublimation for billions of years, in which case they could represent a record of volatile delivery over much of the age of the solar system [Watson et al., 1961]. With its low obliquity and distance from the Sun, the dwarf planet Ceres is a prime candidate for having surface and subsurface ice deposits. Indeed, water ice is probably a primary component of its crust, particularly if Ceres has undergone interior differentiation [Castillo-Rogez and McCord, 2010; McCord et al., 2011]. Both exogenic processes, such as impacts, and endogenic processes, such as faulting or cryovolcanism, could temporarily expose subsurface ice. The thermal stability and lifetime of surface ice is therefore a key question that can be addressed by physical models. Furthermore, volatile deposits have been identified within perennial shadows at the poles of Mercury [Harmon and Slade, 1992; Paige et al., 1992; Harmon et al., 2011] and the Moon [Feldman et al., 2000; Colaprete et al., 2010], motivating the search for similar cold traps on Ceres.

Without an atmosphere, surface heating is driven almost entirely by solar and infrared radiation, such that latitude and obliquity (the angle of the planet's spin axis from the orbit normal) determine temperatures on flat, unobstructed surfaces. However, if the planet's obliquity is small compared to typical topographic slopes, regions of persistent year-round shadow will occur. Here surface temperatures can be much lower than on illuminated surfaces at the same latitude. Indeed, persistently shadowed regions (PSRs) on the Moon and Mercury exhibit a complex morphology determined almost exclusively by topography [Paige et al., 2010; Mazarico et al., 2011]. Thermal conductivity and albedo are also important factors in predicting surface and subsurface temperatures, with reflective, highly conductive ice blocks being much more stable than dust-darkened, porous frost. Temperatures at depths beneath the diurnal thermal "skin depth" (~1 cm for regolith on Ceres) remain near the mean surface temperature, which can be much lower than the peak surface temperature.

Previous investigations suggested that water ice should be thermally stable in Ceres' subsurface over ~30% of the planet, but surface temperatures were thought to be too high for long-term ice survival [Fanale and Salvail, 1989; Schorghofer, 2008; Titus, 2015]. However, these temperature calculations neglected the important effects of topographic shadowing and the nonlinear relationship between maximum and mean temperatures. If temperatures are low enough in persistently shadowed regions at high latitudes, Ceres may indeed possess an extensive yet hidden "ice cap" on its surface, in addition to subsurface ice. Possible signatures of OH and H<sub>2</sub>O emission off the north polar limb of Ceres [A'Hearn and Feldman, 1992; Küppers et al., 2014] could be tantalizing evidence of the seasonal or episodic sublimation of this polar cap. Other more exotic volatiles may also be trapped in the shadowed regions, with the potential to yield information on the primordial composition and delivery of meteoritic material. Subsurface ice may be present at lower latitudes than previously thought, and its excavation by impacts or endogenic processes may lead to observable signatures. Exposed ice on Ceres' surface should have a finite lifetime, even at low latitudes where it is most unstable. In the following sections we investigate temperatures on Ceres with realistic topography, thermophysical properties, and orbital parameters and then explore the implications for ice stability.

## 2. Orbit, Spin State, and Insolation

Insolation at a given latitude  $\lambda$  on a planetary body is determined by its instantaneous distance and orientation with respect to the Sun. Obliquity  $\epsilon$  determines the yearly maximum elevation of the Sun in the sky and the extent of perennial shadow due to topography, such as craters. The orbital eccentricity  $e$  determines the variation in distance to the Sun. The timing of the solar declination  $\delta$  with respect to the perihelion is determined by the "planetocentric longitude of the Sun at perihelion,"  $L_p$ , which dictates how solar irradiance is phased with the seasons in each hemisphere. At a given time  $t$  on a horizontal surface the cosine of the solar incidence angle,  $\mu$ , is

$$\mu = \sin \lambda \sin \delta + \cos \lambda \cos \delta \cos h, \quad (1)$$

where  $h = 2\pi t/P$  is the hour angle, with  $P$  the rotational period (9.08 h for Ceres), and  $t = 0$  at local noon. The solar declination  $\delta$  (i.e., the latitude of the subsolar point) is given by

$$\sin \delta = \sin \epsilon \sin(\nu + L_p), \quad (2)$$

and the true anomaly  $\nu$  is calculated at each time step using the standard formulas of celestial mechanics. The normal solar irradiance at the subsolar point on Ceres depends on its distance  $r$  from the Sun:

$$\begin{aligned} F^*(t) &= \frac{S}{a^2} \left( \frac{a}{r(t)} \right)^2 \\ &= \frac{S}{a^2} (1 + e \cos \nu)^2, \end{aligned} \quad (3)$$

where  $a$  is the orbital semimajor axis in astronomical units (AU). The absorbed solar radiation on the horizontal surface with albedo  $\alpha$  is then

$$F_{\text{solar}} = (1 - \alpha) F^* \mu. \quad (4)$$

To estimate peak insolation, note that at local noon, equations (1) and (2) reduce to

$$\mu = \cos(\lambda - \delta) \approx \cos[\lambda - \epsilon \sin(\nu + L_p)], \quad (5)$$

where the approximation is valid for small values of the obliquity and orbital eccentricity. Note that at the midlatitudes at local noon,  $\mu \approx \cos \lambda$  for small obliquity, and therefore when  $e \ll 1$ , the peak flux simplifies to

$$F_{\text{max}} \approx (1 - \alpha) \frac{S}{a^2} (1 + 2e) \cos \lambda. \quad (6)$$

Ceres' present obliquity has been determined to be  $<10^\circ$ , with a most probable value in the range  $\sim 3\text{--}4^\circ$  [Rambaux et al., 2011]. The most recent results available from the Dawn mission (C. Russell, personal communication, 2015) suggest a nominal obliquity very close to  $3^\circ$ . Using the ephemerides available from the Jet Propulsion Laboratory's Horizons system [Giorgini et al., 1996] (<http://ssd.jpl.nasa.gov/?horizons>), we adopt an orbital eccentricity  $e = 0.0789$ . Although examination of the Horizons ephemeris yields  $L_p = 149^\circ$ , recent data from the Dawn mission indicate that Ceres' axial orientation must be revised (C. Russell,

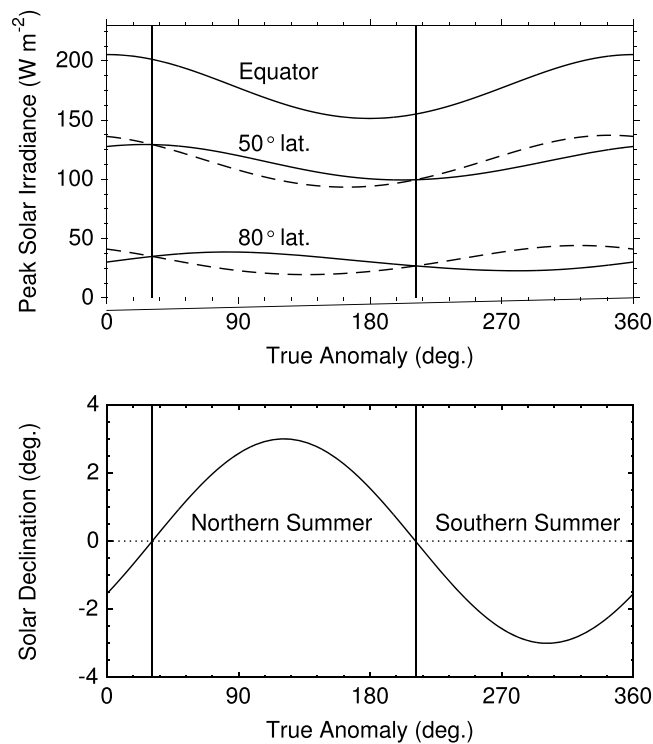


**Figure 1.** Solar irradiance in the northern (solid lines) and southern (dashed lines) hemispheres and solar declination (the subsolar latitude) determine the seasonal distribution of surface temperatures on Ceres. Perihelion occurs during late southern summer, leading to slightly higher peak temperatures in that hemisphere.

personal communication, 2015), such that the true value is  $L_p = 149^\circ - 180^\circ = -31^\circ$ . Perihelion therefore occurs during late southern summer, whereas the northern summer occurs near aphelion (Figure 1), a subtle asymmetry which should also be expressed in the temperature and ice distribution.

Secular perturbations by the planets on the orbital elements of Ceres cause variations in the spin pole and eccentricity, affecting the distribution of incident sunlight. *Bills and Nimmo* [2011] modeled these perturbations (dominated by Jupiter and Saturn) and found Ceres' obliquity to vary with an amplitude of  $\sim 2^\circ$  and a period of  $\sim 40$  kyr. These variations could have a measurable impact on the temperature history and preservation of ice on the surface and interior of Ceres at high latitudes. Obliquity oscillations are probable, but their amplitude is essentially unknown. Secular variations in eccentricity are quite extreme, with a range 0.04–0.12 and period  $\sim 20$  kyr. Meanwhile, spin pole precession and variations of the orbital elements modify  $L_p$ , such that the “cold hemisphere” may alternate between north and south.

### 3. Models

In the following sections we establish a baseline temperature distribution on a smooth “billiard ball” Ceres, beginning with radiative equilibrium (section 3.1) and a one-dimensional heat diffusion model (section 3.2). The 1-D thermal model is then coupled to two sets of surface boundary conditions representing the effects of topography: (1) shadowed portions of simple craters (section 3.3) and (2) rough surfaces with random topography (section 3.4). Finally, we describe the model used for determining ice stability (section 3.5).

#### 3.1. Radiative Equilibrium

The regolith layer on most airless planetary bodies has an extremely low thermal inertia [*Keihm et al.*, 1973], such that sunlit surfaces are very near instantaneous radiative equilibrium. Under this approximation, thermal emission exactly balances absorbed insolation and the surface temperature is given by

$$\bar{\epsilon}\sigma T^4 = (1 - \alpha) \frac{S\mu}{r^2} \equiv F_{\text{solar}}, \quad (7)$$

where  $\alpha$  is the solar albedo,  $\bar{\epsilon}$  the broadband infrared emissivity,  $\sigma$  the Stefan-Boltzmann constant,  $S$  ( $\approx 1361 W m^{-2}$ ) the solar constant,  $r$  the distance to the Sun in astronomical units (AU), and  $\mu$  the cosine of the

solar incidence angle with respect to the surface normal. Peak temperatures calculated in this way are slightly overestimated, due to the nonzero thermal inertia of real materials. Furthermore, at low solar incidence angles, small-scale roughness causes large departures from radiative equilibrium.

A crude estimate of temperatures at depth can be calculated by assuming constant thermal emission balanced against the integrated diurnal insolation, often termed the “planetary equilibrium temperature.” Under this approximation, the mean temperature is given by  $4\bar{\epsilon}\sigma T^4 = F_{\text{solar}}$ , which is smaller than the radiative peak temperature by a geometric factor of  $\sqrt{2}$ . This is an overestimate, because thermal emission during the daytime is much higher than the mean, allowing for more efficient discharge of absorbed solar energy. Nonetheless, the above approximations serve as useful baselines for comparison with the more sophisticated models below.

### 3.2. Thermal Model

The one-dimensional heat diffusion equation governing the variation in temperature  $T$  as a function of time  $t$  and depth  $z$  is

$$\rho c_p \frac{\partial T}{\partial t} = \frac{\partial}{\partial z} \left( K \frac{\partial T}{\partial z} \right), \quad (8)$$

where  $\rho$  is the density,  $c_p$  is the specific heat capacity, and  $K$  is the thermal conductivity of the material. Our thermal model employs a standard finite difference numerical solution [Morrison, 1969] and has been extensively validated with diurnal temperature variations of the Earth’s Moon measured by the Diviner radiometer [Paige et al., 2009; Hayne et al., 2010]. Unless otherwise stated, the models follow the results of Vasavada et al. [2012] and assume that the regolith density increases exponentially with depth:

$$\rho(z) = \rho_d - (\rho_d - \rho_s)e^{-z/H}, \quad (9)$$

with  $H = 6$  cm and the bounding densities  $\rho_s$  and  $\rho_d$  set to 1.0 and 1.7 g/cm<sup>3</sup>, respectively (Table 1). At each depth below the surface, both conduction and radiative transfer between grains result in a temperature- and density-dependent thermal conductivity [Whipple, 1950]:

$$K(T, \rho) = K_c(\rho) + BT^3, \quad (10)$$

with  $B = 4.2 \times 10^{-11}$  W m<sup>-1</sup> K<sup>-4</sup>. The contact thermal conductivity is assumed proportional to density,

$$K_c = K_d - (K_d - K_s) \frac{\rho_d - \rho}{\rho_d - \rho_s}, \quad (11)$$

with  $K_s = 4.0 \times 10^{-4}$  W m<sup>-1</sup> K<sup>-1</sup> and  $K_d = 5.7 \times 10^{-3}$  W m<sup>-1</sup> K<sup>-1</sup>. With these parameters and a temperature-dependent heat capacity following Ledlow et al. [1992], the near-surface thermal inertia  $I = \sqrt{K\rho c_p} \approx 15$  Jm<sup>-2</sup> s<sup>-1/2</sup> K<sup>-1</sup> is consistent with submillimeter light curve observations of Ceres [Chamberlain et al., 2009]. To test the effects of different thermal inertia values, we scale the thermal conductivity at all depths. Table 1 provides a summary of the model parameters used in this study.

Two boundary conditions are required to solve the second-order heat equation; we assume a geothermal flux of  $3 \times 10^{-3}$  W/m<sup>2</sup> at the lower boundary (~5 m depth) and a surface flux accounting for solar and infrared radiation, as described in the following sections. The uppermost layer of the model grid has thickness one tenth of the diurnal skin depth,  $\sqrt{2K/\rho c_p P}$ , and layer thicknesses increase by a factor of 1.2 at each depth. Each model is run with a time step of no greater than 1/400 of a ~9 h Ceres day and allowed to equilibrate for 20 orbits, such that the surface temperature change from year to year is  $\ll 1$  K.

### 3.3. Temperatures Inside Craters

Temperatures inside craters are affected by shadowing, as well as self-heating by absorption of scattered solar and thermal infrared radiation emitted by the illuminated crater wall. Exact analytical solutions for fluxes inside spherical bowl-shaped craters accounting for all orders of scattered and emitted radiation were developed by Buhl et al. [1968]. For craters with small depth-to-diameter ratios  $b$ , Ingersoll et al. [1992] derived the following useful approximation for the incident flux in the craters’ shadowed portions:

$$F_c \approx F_{\text{solar}} [4b^2 (\bar{\epsilon} + \alpha)], \quad (12)$$

which is equal to the instantaneous solar flux on a horizontal surface given in equation (7), multiplied by the factor in brackets. When the Sun is below the horizon ( $\mu < 0$ ), the flux is set to 0. For a typical value of  $b \sim 1/6$  for the smallest lunar craters [Pike, 1977], and assuming  $\bar{\epsilon} = 0.95$  and  $\alpha = 0.09$ , the radiative flux in the shadows at noon is ~10% of the flat-surface flux at the same latitude. An important aspect of equation (12) is that the flux is independent of position within the shadowed part of the crater for this special geometry.

**Table 1.** Baseline Parameter Values Adopted in This Study

Parameter	Symbol	Value	Reference
Solar constant	$S$	$1361 \text{ W m}^{-2}$	<i>Kopp and Lean</i> [2011]
Orbital semimajor axis	$a$	2.77 AU	<i>Giorgini et al.</i> [1996]
Orbital eccentricity	$e$	0.0758	<i>Giorgini et al.</i> [1996]
Obliquity	$\epsilon$	$3^\circ$	<i>Rambaux et al.</i> [2011]
Planetocentric longitude of perihelion	$L_p$	$-31^\circ$	C. Russell (personal communication, 2015)
Infrared emissivity	$\bar{\epsilon}$	0.95	This study.
Solar albedo	$\alpha$	0.09	<i>Li et al.</i> [2006]
Thermal conductivity	$K$	$K_c + BT^3$	<i>Vasavada et al.</i> [2012]
Contact conductivity	$K_c$	$K_d - (K_d - K_s) \frac{\rho_d - \rho}{\rho_d - \rho_s}$	<i>Vasavada et al.</i> [2012]
Surface conductivity	$K_s$	$4.0 \times 10^{-4} \text{ W m}^{-1} \text{ K}^{-1}$	This study.
Deep conductivity	$K_d$	$5.7 \times 10^{-3} \text{ W m}^{-1} \text{ K}^{-1}$	This study.
Radiative conductivity parameter	$B$	$4.2 \times 10^{-11}$	-
Regolith density	$\rho$	$\rho_d - (\rho_d - \rho_s)e^{-z/H}$	<i>Vasavada et al.</i> [2012]
Surface density	$\rho_s$	$1000 \text{ kg m}^{-3}$	This study.
Deep density	$\rho_d$	$1700 \text{ kg m}^{-3}$	This study.
Scale factor	$H$	0.06 m	<i>Vasavada et al.</i> [2012]
Regolith thermal inertia	$I$	$\sim 15 \text{ J m}^{-2} \text{ s}^{-0.5} \text{ K}^{-1}$	<i>Chamberlain et al.</i> [2009]
Latent heat of H <sub>2</sub> O sublimation	$L$	$2.8 \times 10^6 \text{ J kg}^{-1}$	<i>Frederick</i> [2008]
Surface ice stability criterion	$T_{\text{max}}^*$	110 K	<i>Zhang and Paige</i> [2009]
Near-subsurface ice stability criterion	$T_{\text{avg}}^*$	145 K	<i>Schorghofer</i> [2008]
RMS surface slope	$\sigma_s$	$5-25^\circ$	<i>Rosenburg et al.</i> [2011], <i>Bandfield et al.</i> [2015]

### 3.4. Temperatures on Slopes

Rough surfaces on airless bodies experience a broad distribution of temperatures at a range of length scales, due to differences in insolation and absorption of infrared radiation emitted by surrounding terrain [Aharonson and Schorghofer, 2006]. PSRs may be caused by either self-shadowing (slopes angled away from the Sun) or mutual shadowing (one surface casting a shadow on another). Slopes with a pole-facing component  $> \frac{\pi}{2} - |\lambda| + \delta$  may be self-shadowed PSRs, though this depends on the three-dimensional curvature of the surface. At the other extreme, equator-facing slopes may experience much greater peak temperatures than flat terrain at the same latitude. To account for these effects on Ceres' surface temperatures and ice stability, we calculate temperatures for each slope and azimuth pair in a random distribution intended to simulate real topography (see section 4).

For low-albedo bodies such as Ceres, the total flux absorbed by a surface with slope angle  $\eta$  is well approximated as the sum of direct insolation and infrared radiation emitted by surrounding terrain (assumed flat) [Aharonson and Schorghofer, 2006]:

$$F_s \approx F_{\text{solar}} \left[ \frac{\mu_s}{\mu} + \sin^2 \frac{\eta}{2} \right], \quad (13)$$

where the cosine of the solar incidence angle with respect to the local surface normal is

$$\mu_s = \cos \eta \cos \theta - \sin \eta \sin \theta \cos \Delta\psi, \quad (14)$$

$\theta$  is the solar incidence angle with respect to flat ground, and  $\Delta\psi$  is the azimuth angle of the sloped surface with respect to the Sun. When the Sun is below the slope horizon ( $\mu_s < 0$ ), we set  $\mu_s = 0$ . When the Sun is below the flat-ground horizon ( $\mu < 0$ ), we calculate the incident flux from the ground assuming an isothermal surface. Note that equation (13) is analogous to equation (12) but with a different coefficient in brackets.

### 3.5. Ice Stability

A volatile's sublimation temperature is often defined as the point above which 1m of the substance would sublimate in one billion years in vacuum. The choice of 1 m thickness is arbitrary but makes little difference due to the exponential dependence of sublimation rate on temperature. Water ice has a sublimation temperature

of  $\sim 110$  K under vacuum [Vasavada *et al.*, 1999]. Sublimation temperatures for many other important solar system volatiles are given by Zhang and Paige [2009]. The insulation of a dust layer, such as a sublimation lag, affords greatly enhanced thermal stability; ice beneath  $\sim 1$  m of porous regolith can survive temperatures of  $\sim 145$  K for more than a billion years [Schorghofer, 2008].

Sublimation rates are calculated using the following standard formula [Estermann, 1955]:

$$\dot{E} = p_v(T) \sqrt{m / (2\pi RT)}, \quad (15)$$

where  $p_v(T)$  is the equilibrium vapor pressure of ice at temperature  $T$ ,  $m$  is the molecular mass, and  $R$  is the universal gas constant. For a layer of ice at the surface, sublimation removes latent heat  $L$ , such that the modified surface energy balance (equation (7)) becomes

$$\bar{\epsilon} \sigma T^4 = F_{\text{solar}} - L\dot{E}. \quad (16)$$

A full theoretical treatment of volatile sublimation and vapor diffusion is given by Schorghofer [2007] and Schorghofer and Taylor [2007]. For simplicity in this study, we considered subsurface ice ( $< 1$  m depth) to be stable at locations where  $T_{\text{avg}} < 145$  K, consistent with the results of Schorghofer [2008]. To quantify outgassing rates, we also considered the sublimation of ice beneath porous regolith [cf. Fanale and Salvail, 1989; Schorghofer, 2007],

$$\dot{E}_b = D_K \frac{\Delta p}{h} \frac{8}{\pi \bar{v}^2} \sim \frac{d}{h} \dot{E}, \quad (17)$$

where  $D_K$  is the Knudsen diffusion coefficient,  $\Delta p$  is the vapor pressure drop from the sublimation layer to the surface ( $\Delta p \sim p_v(T)$ ),  $h$  is the thickness of the regolith layer, and  $d$  is the effective regolith grain diameter. The approximation on the right-hand side is accurate to within a factor  $\sim 2$  for typical regolith properties, and  $d/h \sim 10^{-4}$  for a 1 m dry regolith layer overlying ice.

## 4. Topography

Although detailed shape models of Ceres may be forthcoming, we can make inferences about the statistical nature of Ceres' topography as it relates to temperature.

### 4.1. Shape and Roughness

In contrast to most other bodies in the asteroid belt, Ceres' shape is nearly spheroidal, with a small polar flattening  $\approx 7\%$  [Thomas *et al.*, 2005]. The planetographic latitude  $\lambda$  on horizontal surfaces is therefore increased by a small amount given by  $\tan \lambda \approx 1.16 \tan \phi$ , where  $\phi$  is the planetocentric latitude. For the temperature calculations, the fluxes are calculated using the planetographic latitude, which properly accounts for the local insolation on a spheroidal body. Topography and surface roughness on a range of scales strongly affect local temperatures. To simulate these effects, the problem is reduced to weighting the set of temperatures calculated for each slope/azimuth pair by their associated probabilities.

Surface roughness on airless bodies is typically dominated by impact cratering on scales of many kilometers down to millimeters [Oberbeck, 1975]. Surface modification by endogenic processes has so far not been observed in the asteroid belt, though Ceres is perhaps the best candidate for such activity [McCord *et al.*, 2011]. Over time, the impact process tends to generate a surface height distribution that is roughly Gaussian, with a scale-dependent root-mean-square (RMS) slope  $\sigma_s$  [Helfenstein and Shepard, 1999]. For the yet unknown small-scale topography of Ceres, we assume an isotropic Gaussian distribution of surface slopes, equivalent to a Rayleigh distribution for the slope magnitude  $s = |\nabla z| = \tan^{-1} \eta$ , given by [Aharonson and Schorghofer, 2006]

$$P(s) ds = \frac{2s}{\sigma_s^2} e^{-s^2/2\sigma_s^2} ds. \quad (18)$$

This distribution is a common consequence of various surface processes such as random superposition of craters and is appropriate for various bodies at various spatial scales [Helfenstein and Shepard, 1999; Aharonson and Schorghofer, 2006; Bandfield and Edwards, 2008]. The slope distribution's width is parameterized by  $\sigma_s$ , the RMS slope. The precise distribution of slopes on Ceres may differ somewhat from this assumption, and the value of  $\sigma_s$  is unknown; hence, we produce results for a range of values consistent with observations of Ceres and other airless bodies.

On the Moon, RMS slopes are typically 5–15° on a scale of ~17 m, with higher values for the older highlands terrains battered by impacts [Rosenburg *et al.*, 2011]. Laser ranging and stereogrammetry of the ~7km radius asteroid 433 Eros revealed RMS slopes of ~10° on the ~0.1–1 km scale [Zuber *et al.*, 2000] and ~10–20° on meter scales [Cheng *et al.*, 2002]. Roughness typically increases with decreasing spatial scale. Stereogrammetry from the Apollo missions suggests lunar surface roughness with RMS slopes of ~10–30° on the centimeter to millimeter scale [Helfenstein and Shepard, 1999], consistent with recent thermal phase curves from the Diviner instrument [Hayne *et al.*, 2012; Bandfield *et al.*, 2015]. Thermal infrared phase curves of Ceres suggest extreme RMS slopes ~44° [Spencer, 1990], although these observations are biased toward the smallest scales over which thermal gradients occur during daytime, scales  $\ll 1$  m. We therefore modeled surface temperatures for rough surfaces with RMS slopes in the range 0°–45° but focus on the results for 5°–25°, which are representative of the expected roughness on scales of meters to kilometers on Ceres.

#### 4.2. Cratered Terrain

If Ceres' surface topography is dominated by impact craters, temperatures within PSRs are dependent on the crater depth-diameter ratio  $b$ , as indicated by equation (12). Shadows within shallower (i.e., smaller  $b$ ) craters tend to have lower temperatures, due to the smaller angular size of the illuminated portion of the crater, as viewed from the shadowed region. In calculating temperatures in these PSRs, we assume that Ceres' crater depth-diameter ratio distribution is close to that of Vesta [Vincent *et al.*, 2014], with a peak at  $b \sim 0.16$ . The fractional area of perennial shadow in lunar craters was derived as a function of latitude and crater size by Bussey *et al.* [2003], who found this fraction to be only weakly dependent upon crater size. We denote this fraction  $x_s(\lambda)$  and estimate the PSR area in the "cap" poleward of latitude  $\lambda_0$  by

$$f_{\text{PSR}}(\lambda > \lambda_0) = \frac{f_c}{1 - \sin(\lambda_0)} \int_{\lambda_0}^{90^\circ} x_s(\lambda) \cos(\lambda) d\lambda, \quad (19)$$

where  $f_c$  is the fractional surface area occupied by craters containing PSRs. For Ceres, we have no a priori constraint on  $f_c$ , so we use the known value for the Moon of  $f_{\text{PSR}} = 5\%$  for  $\lambda_0 = 80^\circ$  [Bussey *et al.*, 2003] and solve equation (19) to derive  $f_c \approx 8\%$ . This value of  $f_c$ , calibrated from the lunar polar regions, indicates that 8% of the surface is covered by craters producing PSRs. The fact that this fraction is substantially smaller than 1 may be understood as resulting from several factors such as the following: larger, shallower craters produce less shadow than smaller, steeper craters; ejecta blankets associated with craters produce plains, diminishing shadows; and any mass wasting processes smooth topography and further reduce the shadow fraction.

Adopting an appropriate value of  $f_c$  for Ceres, the fractional surface area occupied by PSRs can be evaluated at any latitude, using  $f_{\text{PSR}}(\lambda) = f_c x_s(\lambda)$ . We then calculate the temperature distribution  $n(T)$  at each latitude using the flux boundary condition given by equation (12), convolved with the probability distribution for  $b$ . The fractional area  $N$  with  $T_{\text{max}} < 110$  K or  $T_{\text{avg}} < 145$  K can be calculated by simply integrating the temperature probability distribution  $n = \partial N / \partial T$  over the desired range:

$$N(T < T^*) = \int_0^{T^*} n(T) dT. \quad (20)$$

## 5. Results

### 5.1. Smooth Surface Temperatures

At Ceres' mean orbital distance of ~2.77 AU, and with typical values of  $\alpha = 0.09$ ,  $\bar{\epsilon} = 0.95$ , and  $S = 1361$  W/m<sup>2</sup>, equation (7) yields peak temperatures on flat ground as a function of  $\mu$ , the cosine of the solar incidence angle:

$$T_{\text{max}} \approx (243 \text{ K}) \mu^{1/4}. \quad (21)$$

Thus, for the accepted value of Ceres' obliquity of ~3°, peak temperatures on level surfaces with low thermal inertias are expected to range from 243 K near the equator to ~116 K near the poles. At these temperatures, water ice is not expected to persist on level surfaces at any latitude on billion-year time scales. However, the radiative equilibrium approximation overestimates peak temperatures, due to neglecting downward heat conduction. Using the more realistic 1-D thermal model yields the surface temperature curves shown in Figure 2, for different values of latitude, thermal inertia, and albedo. Variations in these parameters can strongly influence surface temperatures. Figures 3 and 4 show the modeled diurnal maximum and mean temperatures over the course of an orbital cycle.

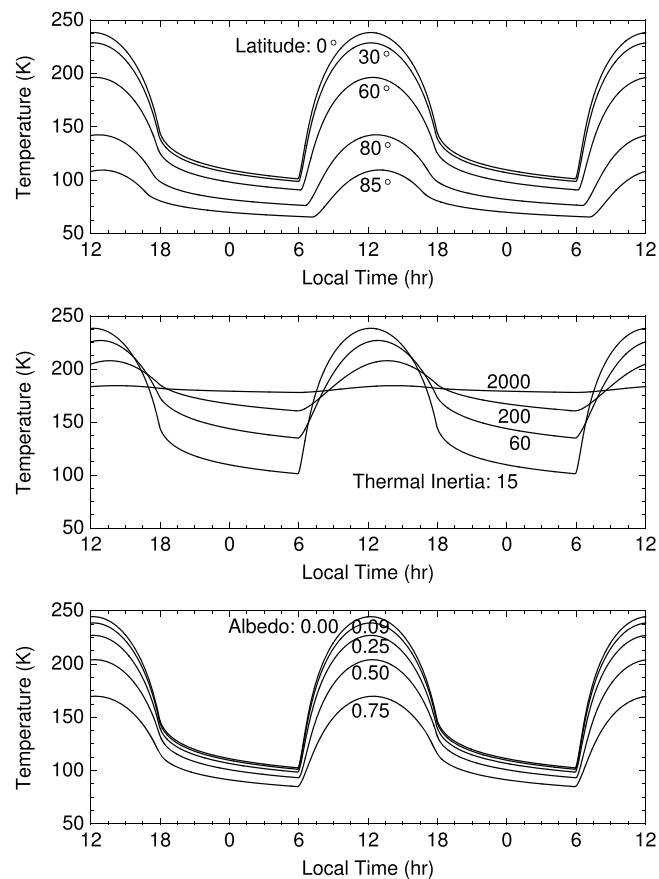


**Figure 2.** Surface temperatures on Ceres at perihelion, calculated for several different values of three different parameters: (top) latitude, (middle) thermal inertia, and (bottom) albedo.

### 5.2. Lifetime of Ice in Sunlight

A self-preserving effect may occur if an ice deposit has an albedo much higher than Ceres' average. For example, water ice with  $\alpha = 0.5$  should have a peak surface temperature reduced by  $\sim 15\%$ , yielding a range 100–210 K, in which case surface ice could be stable against sublimation for billions of years within  $<4^\circ$  of the poles. Figure 5 shows that obliquity exerts a strong influence on the latitude extent of polar ice on Ceres' illuminated surface. For example, if Ceres had near-zero obliquity at some time in the past, then illuminated polar ice caps with high albedo could exist at both poles down to  $\sim 81^\circ$  latitude. However, if Ceres has experienced obliquity excursions exceeding  $5^\circ$  in the geologically recent past (i.e., on a shorter timescale than the effective supply rate), then any surface ice would have sublimated as the ice table retreated to the subsurface. Similarly, a reduction in surface albedo due to lateral mixing by impacts could reduce the stability of a putative polar cap, as shown in Figure 5.

At lower latitudes, ice exposed at the surface rapidly sublimates. Results of our numerical simulations including ice sublimation (equation (16)) are shown in Figure 6. We define ice lifetime as the time to sublimate 1 m of pure ice in vacuum. Both albedo and thermal inertia exert a strong influence on ice lifetime, due to the nonlinear dependence of sublimation rate on temperature. As shown above, an ice deposit with properties typical of Ceres ( $\alpha = 0.09$  and  $I = 15 \text{ J m}^{-2} \text{ K}^{-1} \text{ s}^{-1/2}$ ) is unlikely to survive anywhere on Ceres' illuminated surface for  $> 10^9$  years. With slightly more favorable values,  $\alpha = 0.1$  and  $I = 20 \text{ J m}^{-2} \text{ K}^{-1} \text{ s}^{-1/2}$ , the numerical simulation shows that ice is stable at the illuminated surface for  $10^9$  years at latitudes  $> 88^\circ$ . Increasing the thermal inertia by a factor of 100 permits stable surface ice at latitudes  $> 81^\circ$ ; a similar effect can be achieved by increasing the albedo to  $\sim 0.6$ .

At low latitudes ( $< 45^\circ$ ), ice is stable under illumination only briefly if it has low albedo and low thermal inertia. However, as shown in Figure 6, ice lifetimes at these latitudes can range from  $\sim 10$  years up to  $\sim 10^9$  years, depending on albedo and thermal inertia. For instance, at  $30^\circ$  latitude, an ice deposit with  $\alpha = 0.6$



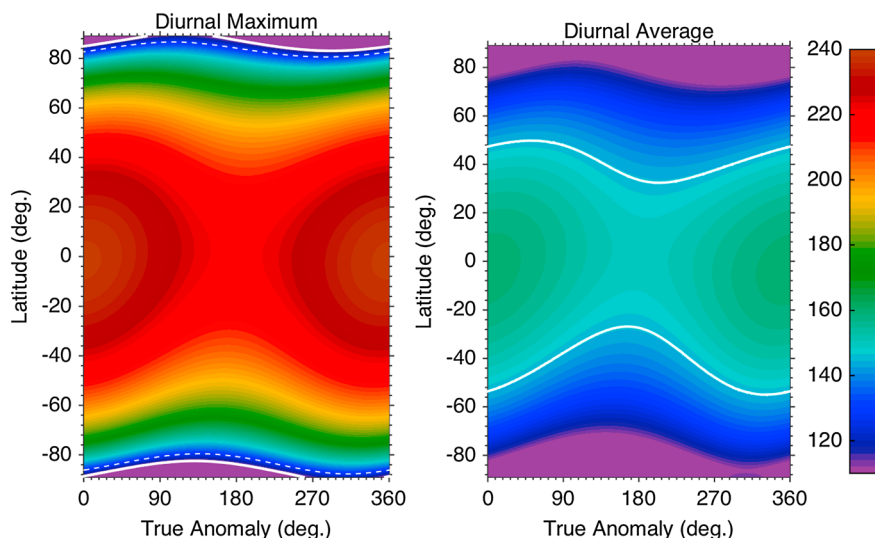


**Figure 3.** Maximum and average diurnal temperatures on Ceres calculated from the 1-D thermal model, as a function of true anomaly. The strong seasonal wave in both panels is primarily due to variations in distance to the Sun caused by orbital eccentricity. (left) Surface ice stability is controlled by maximum surface temperatures ( $< 110$  K, white lines), whereas (right) subsurface temperature controls buried ice stability ( $< 145$  K, white lines). The dashed white line in Figure 3 (left) indicates the stability contour for surface ice with a higher albedo of 0.5.

(comparable to Europa’s cleanest surface ice) could survive for  $\sim 100$  years up to  $> 10^4$  years, depending on its thermal inertia. As the surface darkens by space weathering and contamination by dust, the expected lifetime rapidly decreases. Table 2 summarizes these results for several representative cases.

### 5.3. Cold Traps on Slopes

We calculated surface temperatures for the full range of slopes and azimuths at all latitudes using the flux boundary condition described in section 3.4. Convolution of the resulting temperatures with the slope probability distribution (for a given RMS slope) gives the area-weighted temperature distribution at each latitude (Figure 7). The most likely values of  $T_{avg}$  and  $T_{max}$  at each latitude  $\lambda$  closely follow the function  $T(\lambda) = T_0 \cos^{1/4} \lambda$  for small values of the surface roughness. Best fit values of  $T_{0,avg}$  and  $T_{0,max}$  are consistent at 155 K and 243 K at the equator and generally follow the expected  $\cos^{1/4} \lambda$  behavior. However, surface roughness broadens the temperature distribution and increases the typical peak temperature.

It should be emphasized that the rough surface model does not include any permanent shadowing, due to the fact that each surface facet is considered in isolation. In other words, self-shadowing is included, but mutual shadowing is not included in the model. Nonetheless, Figure 7 shows substantial area with  $T_{max} < 110$  K

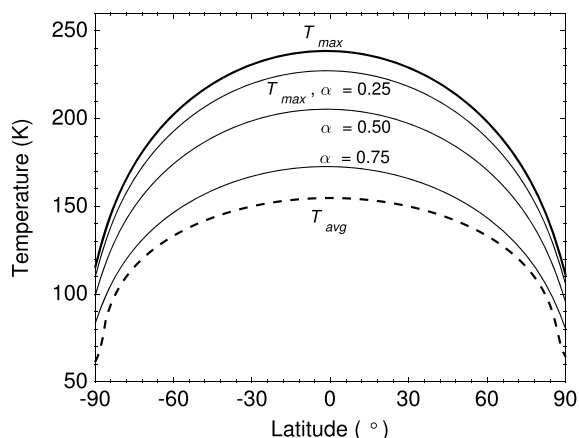


**Figure 4.** Modeled annual maximum and average temperatures on Ceres. Dark solid line shows albedo = 0.09, and the thin solid lines show three higher albedo values.

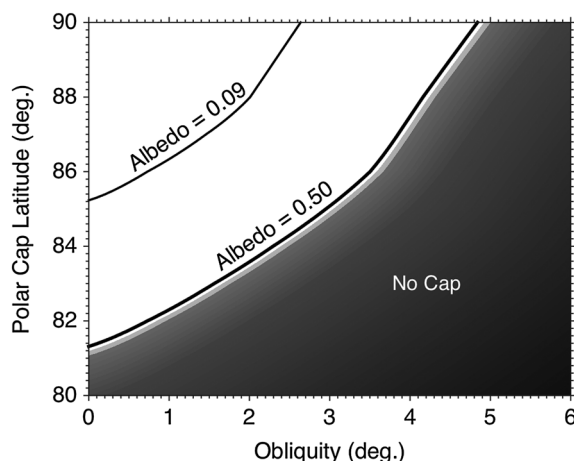


**Figure 5.** The extent of thermal stability for polar water ice on the illuminated (level) surface of Ceres, for a range of obliquity values and two different albedo values, 0.09 (nominal) and 0.50 (fresh ice-like). For obliquities above  $\sim 5^\circ$ , porous water ice is not stable anywhere on Ceres' directly illuminated surface. An exception is the case of cohesive ice, which has a much higher thermal inertia.

(stable surface ice) and  $T_{\text{avg}} < 145 \text{ K}$  (stable buried ice). Because this model only includes illuminated slopes, the derived fractional cold trap area should be considered a lower limit.

#### 5.4. Cold Traps in Craters

By analogy with the Moon and Mercury, it is likely that PSRs on Ceres at scales  $> 100 \text{ m}$  are mostly found in craters. We therefore estimate the temperatures and fractional area of PSRs using equation (19). The crater depth-diameter ratio distribution is assumed to be similar to that of Vesta (Figure 8). Temperatures in the PSRs are calculated using the flux boundary condition from equation (12). The resulting distribution of temperatures in the PSRs over all latitudes is shown in Figure 9. Here the fractional area has been weighted by the PSR fraction  $x_s$  for each value of  $b$  and normalized at each latitude bin. The sharp latitude cutoff is due to the fact that  $x_s \rightarrow 0$  at  $\sim 63^\circ$  for  $b \sim 1/6$ . In reality, we expect a smoother transition due to the presence of PSRs in very steep-walled craters below this latitude, but these contribute negligibly to the cold trap area.

Integrating the temperature distribution with equation (20) gives a cumulative distribution function (CDF) representing the fractional surface area with temperature below a given value  $T^*$ . Again, we choose  $T_{\text{max}}^* = 110 \text{ K}$  as the stability criterion for surface ice and  $T_{\text{avg}}^* = 145 \text{ K}$  as the buried ice stability criterion. Figure 10 shows the CDF for these two criteria as a function of latitude and three values of the RMS slope ( $5^\circ$ ,  $15^\circ$ , and  $25^\circ$ ). Buried ice is stable within  $\sim 1 \text{ m}$  of the surface starting at latitude  $\sim 40^\circ$ , with a latitude profile that depends on surface roughness; higher RMS slope leads to buried ice stability over a broader range of latitudes. Surface ice becomes stable at latitudes higher than  $\sim 60^\circ$  within persistent shadows on steep slopes and within PSR craters. Rougher surfaces lead to a broader latitude distribution of surface cold traps on self-shadowed slopes. PSRs within craters dominate the cold trap surface area for low RMS slope values, but very rough surfaces (e.g., RMS slope  $\sim 25^\circ$ ) can contribute comparable surface area. At the highest latitudes the surface and subsurface cold trap area also decreases with increasing RMS slope, because of the heating by adjacent surfaces and increased prevalence of steep equator-facing slopes. The cumulative cold trap area fraction  $A(T < T^*)$  is shown in Figure 11. On self-shadowed slopes,  $A(T < 110 \text{ K})$  is  $\sim 10^{-4}$  to  $10^{-3}$ , depending on surface roughness. Cold traps for  $\text{H}_2\text{O}$  ice within all PSR craters are predicted to occupy  $\sim 10^{-3}$  (0.1%, or  $\sim 5 \times 10^3 \text{ km}^2$ ) of Ceres' total surface area.

## 6. Discussion

### 6.1. Volatile Distribution and Composition

The results above show that temperatures on a smooth billiard ball Ceres are expected to be too high to maintain water ice at the sunlit surface over billion-year time scales if the albedo is uniformly 0.09. However, if supply rates are high enough for surface ice to maintain a relatively high albedo ( $\sim 0.5$ ), then contiguous, illuminated ice caps may persist within a few degrees of the poles for  $> 1 \text{ Gyr}$  (provided  $\epsilon < 5^\circ$ ). Similarly, ice on the illuminated surface at the low to middle latitudes may persist up to  $\sim 10^4$  years, if it maintains a high

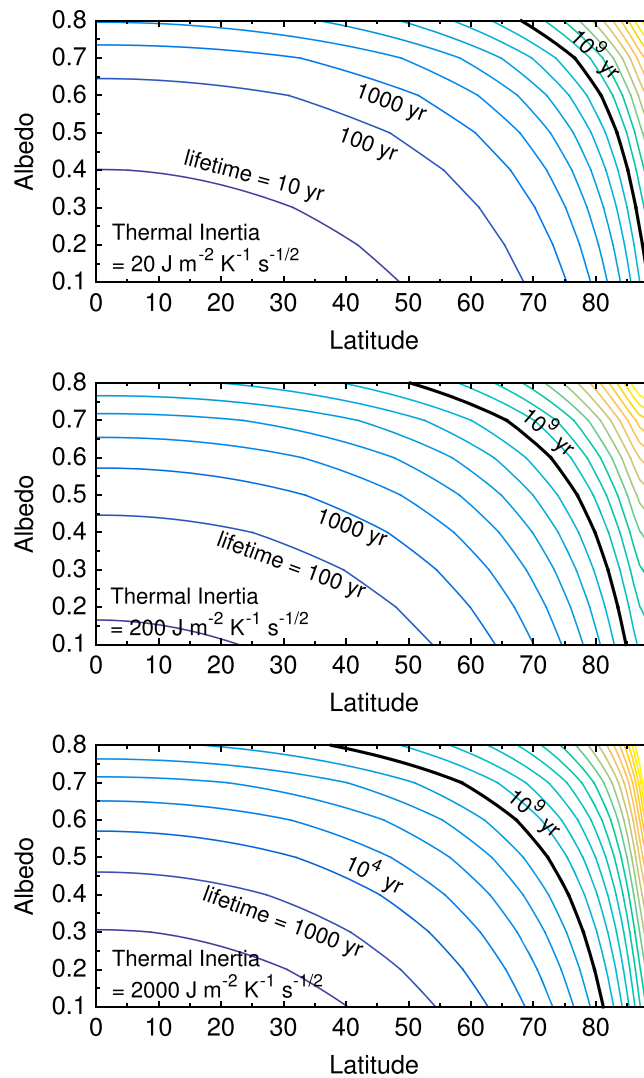


**Figure 6.** Lifetime of ice on the surface of Ceres, including the effects of latent heat of sublimation, albedo, and thermal inertia. Each panel shows contours of ice lifetime (i.e., the time to sublimate 1 m of ice) as a function of latitude and albedo, for three different values of the thermal inertia. A thermal inertia of  $20 \text{ J m}^{-2} \text{ K}^{-1} \text{ s}^{-1/2}$  is comparable to the typical Ceres regolith, whereas a value of 2000 is equivalent to a cohesive block of ice.

albedo and high thermal inertia. Such properties would be typical of cohesive blocks of nearly pure ice but not granular ice, particularly if it becomes coated in dust. As an example, dusty, granular ice with albedo 0.1 and thermal inertia  $20 \text{ J m}^{-2} \text{ K}^{-1} \text{ s}^{-1/2}$  could be thermodynamically stable at  $85^\circ$  latitude for 4 Myr.

Using more realistic topography, shadows substantially expand the fraction of Ceres' surface and subsurface where water ice is stable. Both self-shadowed slopes and PSRs within craters become cold enough to trap water ice at the surface at latitudes  $>60^\circ$ . A widespread subsurface ice table within  $\sim 1$  m depth is stable at latitudes  $>40^\circ$  (Figure 10).

Interestingly, a significant fraction of the cold trap area on Ceres is likely to be cold enough to trap other volatiles in addition to water ice. Some of the relevant volatiles for which *Zhang and Paige* [2009] have cataloged sublimation temperatures include methanol ( $\text{CH}_3\text{OH}$ , 90 K), ammonia ( $\text{NH}_3$ , 66 K), sulfur dioxide ( $\text{SO}_2$ , 62 K), carbon dioxide ( $\text{CO}_2$ , 54 K), hydrogen sulfide ( $\text{H}_2\text{S}$ , 50 K), methane ( $\text{CH}_4$ , 22 K), and carbon monoxide ( $\text{CO}$ , 18 K). Note that these sublimation temperatures are standardized to a loss rate of  $1 \text{ mm yr}^{-1}$ . All of these compounds are known constituents of comets and other primitive bodies and, therefore, may be present in some form on Ceres. All are more volatile than water and are not stable anywhere on Ceres' sunlit surface but may be cold trapped in the shadows. The modeled surface areas of stability for these volatiles are tabulated in Table 3.

**Table 2.** Lifetime of Illuminated Water Ice on Ceres

Latitude	Albedo	Thermal Inertia ( $J m^{-2} K^{-1} s^{-1/2}$ )	$T_{max}$ (K)	Peak Sublimation Rate ( $kg m^{-2} s^{-1}$ )	Lifetime ( $yr m^{-1}$ )
0°	0.1	20	190	$4.4 \times 10^{-5}$	4
	0.5	20	183	$1.3 \times 10^{-5}$	18
	0.5	2000	157	$5.5 \times 10^{-8}$	$2 \times 10^3$
30°	0.1	20	188	$3.2 \times 10^{-5}$	5
	0.5	20	180	$7.6 \times 10^{-6}$	30
	0.5	2000	152	$1.6 \times 10^{-8}$	$7 \times 10^3$
60°	0.1	20	182	$1.1 \times 10^{-5}$	22
	0.5	20	169	$8.5 \times 10^{-7}$	670
	0.5	2000	133	$5.2 \times 10^{-11}$	$2 \times 10^6$
85°	0.1	20	139	$3.7 \times 10^{-10}$	$4 \times 10^6$
	0.5	20	118	$1.6 \times 10^{-13}$	$1 \times 10^{10}$
	0.5	2000	90	$1.7 \times 10^{-20}$	$1 \times 10^{16}$

In regions of perennial shadow, temperatures are controlled by scattered sunlight and emitted infrared radiation from other surfaces, as well as heat flow from the planetary interior. Small regions of multiple shadowing may exist where the scattered sunlight and infrared radiation is negligible, such that surface temperature is balanced by interior heat flow:  $T_{min} \approx (Q/\epsilon\sigma)^{1/4}$ . Assuming that the radiogenic heat production within Ceres' silicate component falls in the range of  $0.5-1.0 \times 10^{-11} W kg^{-1}$  between ordinary chondrites and Earth's mantle [Wasserburg et al., 1964], and a silicate fraction of 0.75 [McCord et al., 2011], we expect a steady state heat flow  $Q \approx 1 - 3 \times 10^{-3} W m^{-2}$ . The corresponding minimum surface temperature is 12–15 K. Adopting a radiogenic element composition similar to the bulk silicate Earth leads to small differences in minimum temperature. In the absence of nonthermal loss mechanisms, water plus all of the “supervolatiles” listed above may persist on such surfaces for the age of the solar system, if Ceres' obliquity has remained  $<5^\circ$ .

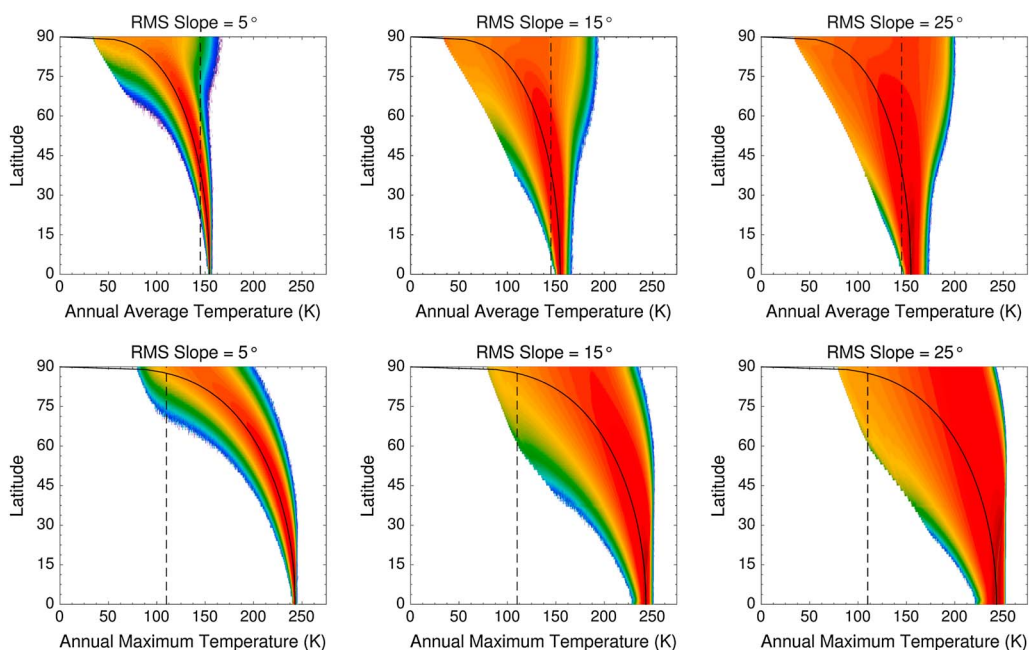


**Figure 7.** Histograms of annual (top row) average and (bottom row) maximum temperatures, where colors indicate the base10 logarithm of the fractional area within each  $1^\circ$  latitude bin, with blue-purple being low and red-brown being high. The black lines are functions of the form  $T = T_0 \cos^{1/4} \lambda$ . RMS slope is a measure of surface roughness, corresponding to the peak in the Gaussian distribution of slopes.

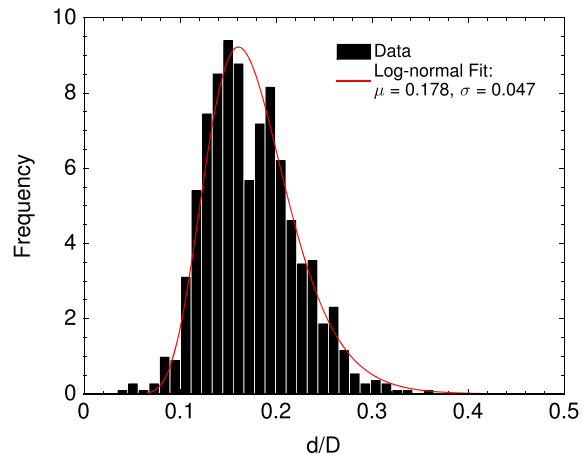


**Figure 8.** Crater depth-diameter distribution on Vesta (data from Vincent *et al.* [2014]), fitted with a lognormal distribution. In this study, we assumed that Ceres follows a similar distribution of crater geometries.

### 6.2. Water Production and Destruction Rates

Observations of H<sub>2</sub>O outgassing by Küppers *et al.* [2014] provide motivation for investigating the implications of the preceding thermal models for the behavior of volatiles on Ceres. Owing to its low surface gravity and large atmospheric molecular mean free path, Ceres loses a large fraction of vapor molecules to thermal (Jeans) escape. This loss process can be quantified by considering the mean thermal velocity,  $\bar{v} = \sqrt{3kT/m}$ , which determines the characteristic timescale for gravitational escape [Watson *et al.*, 1961]:

$$\tau = \frac{\sqrt{6\pi}}{3g} \bar{v} \frac{e^{\gamma}}{Y}, \tag{22}$$

where  $k$  is Boltzmann’s constant,  $g$  is the surface gravity,  $Y = 3v_{\text{esc}}^2/2\bar{v}^2$ , and  $v_{\text{esc}} \approx 510 \text{ m s}^{-1}$  is the escape velocity. For water, we find  $\tau \sim 10^4 \text{ s}$ . On any single “hop” from one location to another, the probability of escape is then  $\beta = 1 - e^{-t/\tau}$ , where  $t = \sqrt{2}\bar{v}/g$  is the mean flight time. The statistical model of Watson *et al.* [1961] can be used to place an upper limit on the escape rate from the surface cold traps:

$$\dot{M}_s = fA\dot{E}(1 - \gamma), \tag{23}$$

where  $\gamma = \beta / (f(1 - \beta) + \beta)$ ,  $f$  is the fraction of Ceres’ total surface area  $A$  occupied by the cold traps (Table 3), and  $\dot{E} = p_v/\bar{v}$  is the maximum sublimation rate into vacuum at the equilibrium vapor pressure  $p_v(T)$ . In the case of 15° RMS surface slope, our calculations in the preceding sections yield  $fA \sim 9 \times 10^3 \text{ km}^2$  with peak

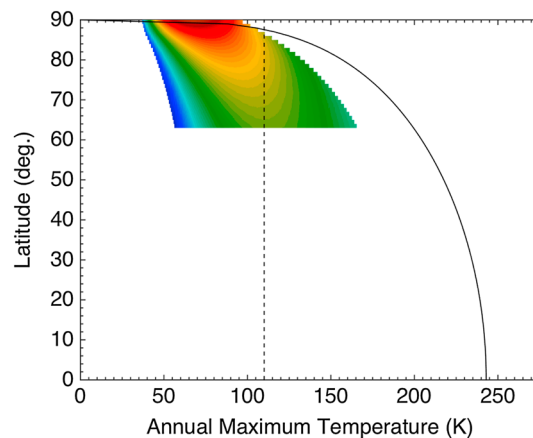


**Figure 9.** Annual maximum temperature histogram for PSRs within craters, where colors indicate the fractional area within each latitude bin, with blue-purple being low and red-brown being high. The black line is the function  $T = T_0 \cos^{1/4} \lambda$ , with  $T_0 = 243 \text{ K}$ , which corresponds to peak temperatures on illuminated horizontal surfaces with zero thermal inertia.

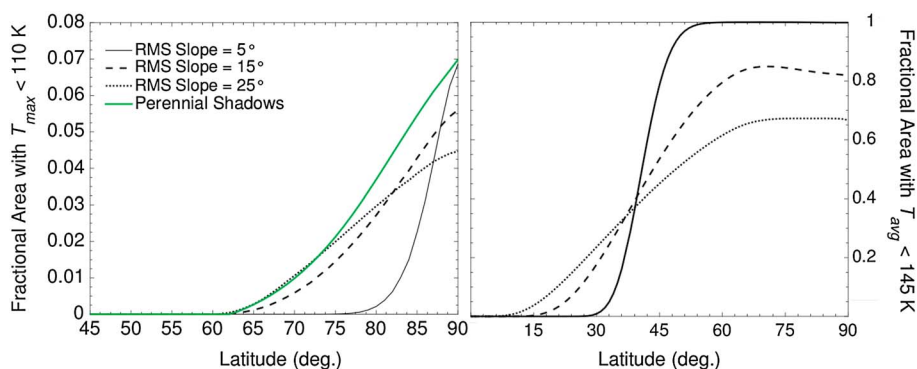


**Figure 10.** Fractional surface area with (left) maximum temperatures < 110 K and (right) average temperatures < 145 K, which are stability criteria for surface and subsurface ice, respectively. All perennial shadows have average temperatures < 145 K.

temperature < 110 K, such that  $\dot{M}_s < 3 \times 10^{-5} \text{ kg s}^{-1}$ . This is an upper limit on the steady state outgassing rate from the cold traps and accounts for the fact that some fraction of the sublimated molecules recondense. If the source flux of water molecules to Ceres' polar regions (either exogenic or endogenic) is higher than this outgassing rate, then H<sub>2</sub>O will accumulate in the cold traps.

Other important destruction processes affecting surface volatile deposits include photodissociation, photoionization, and sputtering by cosmic rays and micrometeorite impacts. On the Moon and Mercury, the most important of these is photodestruction [Butler, 1997], with a characteristic time constant of  $\sim 10^4 - 10^5$  s. Scaling the solar flux to the orbit of Ceres, we expect a photodestruction timescale  $\sim 10^5 - 10^6$  s, which is much longer than the timescale of gravitational loss. Indeed, a Monte Carlo model of water molecules in Ceres' exosphere [Tu et al., 2014] found a mode dynamical lifetime of  $\sim 10^4$  s, very similar to the gravitational escape timescale. Tu et al. [2014] also found that the majority of H<sub>2</sub>O molecules on ballistic trajectories are eventually deposited in the cold traps, with a marked preference for the winter pole.

Sublimation of ice on Ceres' illuminated surface is an interesting possible explanation for outgassing of H<sub>2</sub>O recently detected by Küppers et al. [2014] (Figure 12). Those authors estimated an outgassing rate of  $\sim 6 \text{ kg s}^{-1}$  to explain their observations. The steady state flux from the cold traps (see above) is therefore far too low to explain the observed water vapor. If the outgassing is episodic, then this is not surprising, because H<sub>2</sub>O molecules should be trapped in the coldest parts of the planet, where temperatures are consistently < 110 K and sublimation is negligible. Another possibility is the sublimation of recently exposed ice at lower latitudes. Table 2 provides peak sublimation rates for exposed ice at several latitudes. For example, at 30° latitude, the surface area of granular ice required to produce the  $\sim 6 \text{ kg s}^{-1}$  is  $\sim 0.8 \text{ km}^2$  if its albedo is 0.5. Due to the nonlinear dependence of sublimation rate on temperature, most of this sublimation would occur near perihelion. However, at such high sublimation rates, surface ice must be replenished on decade timescales.

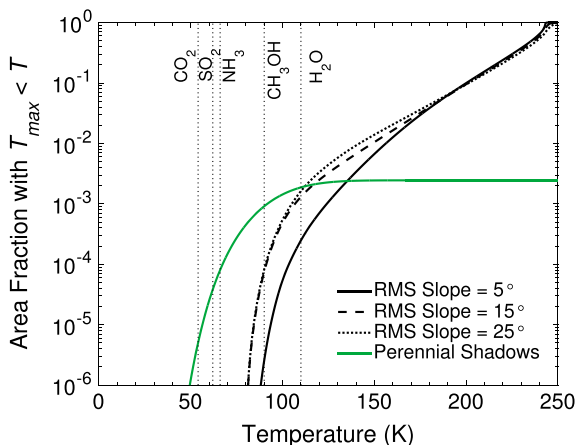


**Figure 11.** Cumulative distribution function for surface area with  $T_{\text{max}} < 110 \text{ K}$ , the stability criterion for surface ice.

**Table 3.** Total Surface Areas of Thermal Stability for Each Volatile Species and Three Values of RMS Slope

Species	$T_{sub}$ (K)	Stable Area ( $\times 1000 \text{ km}^2$ )		
		5°	15°	25°
H <sub>2</sub> O	110	5.9	8.8	9.7
CH <sub>3</sub> OH	90	2.5	2.7	2.8
NH <sub>3</sub>	66	0.22	0.22	0.22
SO <sub>2</sub>	62	0.11	0.11	0.11
CO <sub>2</sub>	54	0.01	0.01	0.01
H <sub>2</sub> S	50	-	-	-
CH <sub>4</sub>	22	-	-	-
CO	18	-	-	-
N <sub>2</sub>	16	-	-	-

A more cohesive ice deposit would persist longer but would also have a slower sublimation rate, requiring greater surface area to explain the observed outgassing. For example, increasing thermal inertia to  $2000 \text{ J m}^{-2} \text{ K}^{-1} \text{ s}^{-1/2}$  yields a required surface ice-covered area of  $> 2 \times 10^3 \text{ km}^2$  at  $30^\circ$  latitude.

Outgassing from the subsurface is another possible explanation for the observed H<sub>2</sub>O vapor around Ceres. An estimate of the outgassing rate is obtained by integrating  $\dot{E}_b$  from equation (17) over all latitudes where subsurface ice is stable, i.e.,  $>50^\circ$ , accounting for the variable temperatures at the ice table. *Fanale and Salvail* [1989] did this calculation, by modeling mean annual temperatures on a smooth Ceres, and found  $\dot{M}_b = \int \dot{E}_b dA \sim 0.1 - 1 \text{ kg s}^{-1}$  for the entire globe. Including surface roughness effects, we found that the latitude range of subsurface ice stability increases, but the outgassing rate is increased by no more than a factor  $\sim 2$ . This suggests that the background outgassing rate may be just below the detection limit of *Küppers et al.* [2014].

An upper limit on seasonal outgassing rates can be estimated by considering the latitude band where buried ice is seasonally stable,  $\sim 30^\circ - 50^\circ$  (Figure 3). The main driver of seasonal temperature variability in this latitude band is the orbital eccentricity, with highest subsurface temperatures  $\sim 155 \text{ K}$  near perihelion. Maximum seasonal heating rates should occur during early southern summer ( $\nu \approx 230^\circ$ ), prior to perihelion. Peak seasonal outgassing rates are constrained to be  $< A\dot{E}_b \sim 1 \text{ kg s}^{-1}$ , with  $A = 4\pi R^2(\cos \lambda_1 - \cos \lambda_2)$  the area of the latitude band  $\lambda_1 = 30^\circ$  to  $\lambda_2 = 50^\circ$ . This maximum outgassing rate is the same order of magnitude as

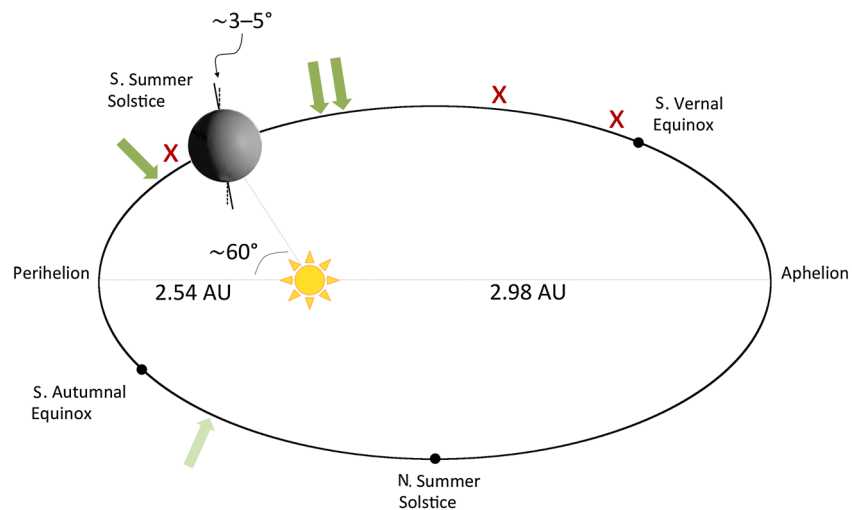


**Figure 12.** Orbit diagram showing Ceres' position and orientation with respect to the Sun and detections of possible outgassing events. Dark green arrows indicate positive detections of H<sub>2</sub>O vapor molecules by *Küppers et al.* [2014], the light green arrow indicates positive detection of -OH emissions by *A'Hearn and Feldman* [1992], and red crosses indicate nondetections.

the observed H<sub>2</sub>O flux near Ceres' perihelion, lending credibility to this hypothesis. However, more detailed modeling is needed to fully quantify the seasonal vapor fluxes through the regolith.

Possible exogenic sources for volatiles include delivery by comets and asteroids and implantation of solar wind ions, which would complement outgassing from the interior. We have few constraints on these processes, but the apparently high ice/rock ratio of Ceres suggests that the interior may be the most important source of water. Based on the mean subsurface H<sub>2</sub>O outgassing rates derived above,  $\dot{M}_b \sim 10^{24} - 10^{25}$  molecules s<sup>-1</sup> globally. The rate of accumulation at the cold traps can be estimated in analogy with equation (23) to be  $\gamma\dot{M}_b \sim 10^{22} - 10^{23}$  s<sup>-1</sup> or  $10^{-3} - 10^{-2}$  kg s<sup>-1</sup>, which is more than sufficient to compensate the sublimation loss  $\dot{M}_b$  calculated above for the shadowed cold traps. Therefore, absent other destruction or burial mechanisms, surface ice would be expected to accumulate in Ceres' PSRs.

## 7. Conclusions

In this study, we investigated temperatures and the stability of ice on the surface and in the near subsurface of Ceres. We considered both smooth surfaces and rough topography, including persistently shadowed craters (PSRs). Modeled annual maximum temperatures on illuminated level surfaces on Ceres range from 243 K at the equator to 116 K near the poles, if heat conduction is negligible (i.e., near-zero thermal inertia). Including vertical heat conduction, annual maximum temperatures range from ~240 K at the equator to ~114 K at the poles. Annual average temperatures on illuminated, level surfaces range from ~160 K to < 100 K, equator to pole. Higher albedo or thermal inertia than Ceres' average values of 0.09 and ~15 J m<sup>-2</sup> K<sup>-1</sup> s<sup>-1/2</sup> could significantly decrease peak temperatures. For example, a surface with albedo 0.5 and thermal inertia 4 times higher (similar to lunar regolith) would reach only ~195 K at the equator. Ceres also experiences a very strong seasonal temperature cycle, primarily driven by orbital eccentricity; peak equatorial daytime temperatures are ~20 K lower at aphelion than at perihelion.

Surface ice is not thermodynamically stable on Ceres' illuminated surface on billion-year timescales, unless it maintains a high albedo and/or high thermal inertia. However, surface ice is only marginally unstable at the poles, such that increasing the albedo by just a few percent could permit a stable polar cap on geological timescales. Volatile resupply would be more rapid than darkening by dust contamination in this case. Similarly, very high albedo ice may persist in sunlight at latitudes <45° for > 10<sup>4</sup> - 10<sup>5</sup> years for a snow-like deposit, or > 10<sup>9</sup> years if it consists of large, cohesive blocks. The absence of a polar ice cap on Ceres is consistent with obliquity excursions to ~5° during the ~40 kyr cycle [Bills and Nimmo, 2011], which would have caused its rapid sublimation. Alternatively, meteorite impacts may have darkened Ceres' surface uniformly, which would render the polar cap invisible, even if it is thermodynamically stable.

Buried ice is stable within ~1m on Ceres at latitudes higher than ~50° (based on the 145 K isotherm), with a slightly greater extent in the northern hemisphere. Seasonal cycles drive latitude oscillations of the 145 K isotherm between ~30° (aphelion) and ~50° (perihelion). Again, albedo and thermal inertia can increase the stability of buried ice. In contrast to the results of Fanale and Salvail [1989], who only modeled daily mean temperatures, our results show that fully modeling the diurnal temperature cycle leads to ~10° greater latitude extent of buried ice. This is due to the enhanced thermal emission to space during daytime, which reduces the net heating at depth.

Roughness on all length scales strongly affects surface and subsurface temperatures on Ceres. In the global view, roughness broadens the temperature distribution (allowing more cold slopes), while shifting the peaks in the histograms of annual maximum and average temperatures higher. We examined these temperature distributions for three plausible values [Rosenburg et al., 2011; Bandfield et al., 2015] of the RMS slope (5°, 15°, and 25°). In all three cases, surface ice is stable to sublimation at latitudes >60°, with a cold trap surface area ~ 0.03–0.2% of Ceres' total surface area, or 0.8 – 5 × 10<sup>3</sup> km<sup>2</sup>. Increasing roughness generally leads to greater cold trap area but also higher maximum temperatures within a latitude band. It should be noted that surface temperatures calculated by our rough surface model do not include mutual shadowing and represent a lower bound on the cold trap surface area.

Persistent year-round shadows within craters (PSRs) can contribute substantially to Ceres' cold trap surface area. At latitudes >60°, the PSRs are considerable, and the majority are perennially <110 K. Above ~85° latitude, all PSRs meet this temperature criterion. Their total surface area is ~ 0.2% of Ceres' total surface area, or ~ 5 × 10<sup>3</sup> km<sup>2</sup>. A conservative upper limit on the cold trap area can be estimated by combining the PSRs with



the contribution of cold, pole-facing slopes above, giving a total area of  $\sim 10^4$  km<sup>2</sup>. At the highest latitudes, PSRs on Ceres are also capable of cold trapping even more exotic volatiles, such as methanol, ammonia, sulfur dioxide, and carbon dioxide. Furthermore, ice in the PSRs could be stable against obliquity excursions to  $>5^\circ$ , unlike ice on the illuminated surface.

Outgassing of H<sub>2</sub>O by sublimation of surface ice is possible in illuminated regions if ice has been recently exposed. From the equator to 30° latitude, ice can survive in direct sunlight for  $> 10^3$  years if it has both high albedo and high thermal inertia. Granular ice can survive for just decades at these latitudes, even with high albedo. To match inferred water vapor fluxes from Küppers *et al.* [2014], a surface area of  $\sim 0.8$  km<sup>2</sup> of sublimating granular ice would be required at low latitudes. However, this ice deposit would need to be refreshed every  $\sim 10$ –100 years. Cohesive ice (high thermal inertia) could supply the required water vapor by sublimation with a surface area of  $\sim 10^3$  km<sup>2</sup> and could persist for  $\sim 10^4$  years.

Vapor diffusion from a buried ice table through the regolith layer to the surface is another plausible explanation for the observed H<sub>2</sub>O and OH around Ceres. The steady state production of H<sub>2</sub>O by this process (already calculated by Fanale and Salvail [1989]) is  $\sim 0.1$ –1 kgs<sup>-1</sup>. This is just below the detection threshold of the observations. However, if we assume that the latitude band traversed by the 145 K isotherm participates in seasonal sublimation, then fluxes can be  $> 1$  kgs<sup>-1</sup>. Therefore, sublimation of buried ice is a plausible explanation for the observed outgassing, although more detailed modeling is needed. Interestingly, our models show that the period of most rapid heating at the ice table should occur prior to perihelion, during the period when the vapor was observed.

Our model results are directly or indirectly testable by data from the Dawn mission. For example, the models predict a near-surface ice table beginning at  $\sim 50^\circ$ , which should be detectable by the Gamma Ray and Neutron Detector experiment. Surface ice deposits, primarily in the shadows, are expected to occupy a small fractional area starting at  $\sim 60^\circ$  if the surface is rough, or higher latitudes if it is smoother than expected. Water ice observed on the visible surface by Dawn should be colder than its surroundings due to both albedo and the latent heat of sublimation. Due to its relative instability on geologic timescales, any water ice detected at low latitudes must have been deposited recently ( $< 10^4$  years) by either exogenic or endogenic processes. At high latitudes, especially  $> 60^\circ$ , subsurface ice excavated by impacts may persist for millions of years on the illuminated surface. If icy impact craters are not observed by Dawn, this would imply either an ice-poor crust or a rapid process of surface darkening, presumably by accumulation of meteoritic infall or a sublimation lag deposit.

#### Acknowledgments

We thank Norbert Schorghofer, Bruce Bills, and Nicolas Rambaux for valuable discussions. Mikhail Kreslavsky and Matthew Siegler provided exceptionally thoughtful reviews, from which the paper benefited immensely. A workshop hosted by Thomas McCord and Julie Castillo-Rogez at the Bear Fight Institute provided the initial inspiration for this study, which was fueled by continued workshops and support from the Weizmann Institute of Science (WIS). Oded Aharonson wishes to acknowledge important support from the Helen Kimmel Center for Planetary Science, the WIS Minerva Center, and ISF I-CORE program. Part of this work was carried out at the Jet Propulsion Laboratory, California Institute of Technology, under contract with the National Aeronautics and Space Administration. Copyright 2015, all rights reserved. The source code and input files for the models used in this study are available from the authors upon request (Paul.O.Hayne@jpl.nasa.gov), pending approval for public release by NASA/JPL.

#### References

- Aharonson, O., and N. Schorghofer (2006), Subsurface ice on Mars with rough topography, *J. Geophys. Res.*, *111*, E11007, doi:10.1029/2005JE002636.
- A'Hearn, M. F., and P. D. Feldman (1992), Water vaporization on Ceres, *Icarus*, *98*, 54–60.
- Bandfield, J. L., and C. S. Edwards (2008), Derivation of Martian surface slope characteristics from directional thermal infrared radiometry, *Icarus*, *193*(1), 139–157.
- Bandfield, J. L., P. O. Hayne, J. P. Williams, B. T. Greenhagen, and D. A. Paige (2015), Lunar surface roughness derived from LRO Diviner Radiometer observations, *Icarus*, *248*, 357–372.
- Bills, B. G., and F. Nimmo (2011), Forced obliquities and moments of inertia of Ceres and Vesta, *Icarus*, *213*, 496–509, doi:10.1016/j.icarus.2010.09.002.
- Buhl, D., W. J. Welch, and D. G. Rea (1968), Reradiation and thermal emission from illuminated craters on the lunar surface, *J. Geophys. Res.*, *73*, 5281–5295.
- Bussey, D. B. J., P. G. Lucey, D. Steutel, M. S. Robinson, P. D. Spudis, and K. D. Edwards (2003), Permanent shadow in simple craters near the lunar poles, *Geophys. Res. Lett.*, *30*(6), 1278, doi:10.1029/2002GL016180.
- Butler, B. J. (1997), The migration of volatiles on the surfaces of Mercury and the Moon, *J. Geophys. Res.*, *102*, 19,283–19,291.
- Castillo-Rogez, J. C., and T. B. McCord (2010), Ceres' evolution and present state constrained by shape data, *Icarus*, *205*, 443–459.
- Chamberlain, M. A., A. J. Lovell, and M. V. Sykes (2009), Submillimeter photometry and light curves of Ceres and other large asteroids, *Icarus*, *202*, 487–501.
- Cheng, A. F., O. Barnouin-Jha, L. Prockter, M. T. Zuber, G. Neumann, D. E. Smith, J. Garvin, M. Robinson, J. Veverka, and P. Thomas (2002), Small-scale topography of 433 Eros from laser altimetry and imaging, *Icarus*, *155*, 51–74, doi:10.1006/icar.2001.6750.
- Colaprete, A., et al. (2010), Detection of water in the LCROSS ejecta plume, *Science*, *330*, 463–468.
- Estermann, I. (1955), Gases at low densities, in *Thermodynamics and Physics of Matter, High Speed Aerodynamics and Jet Propulsion*, vol. 2, edited by F. D. Rossini, pp. 742–744, Princeton Univ. Press, Princeton, N. J.
- Fanale, F. P., and J. R. Salvail (1989), The water regime of Asteroid (1) Ceres, *Icarus*, *82*, 97–110.
- Feldman, W. C., D. J. Lawrence, R. C. Elphic, B. L. Barraclough, S. Maurice, I. Genetay, and A. B. Binder (2000), Polar hydrogen deposits on the Moon, *J. Geophys. Res.*, *105*(E2), 4175–4195, doi:10.1029/1999JE001129.
- Frederick, J. E. (2008), *Principles of Atmospheric Science*, Jones and Bartlett, U. K.
- Giorgini, J. D., D. K. Yeomans, A. B. Chamberlain, P. W. Chodas, R. A. Jacobson, M. S. Keesey, J. H. Lieske, S. J. Ostro, E. M. Standish, and R. N. Wimmerly (1996), JPL's on-line solar system data service, *Bull. Am. Astron. Soc.*, *28*, 1158.

- Harmon, J. K., and M. A. Slade (1992), Radar mapping of Mercury: Full-disk images and polar anomalies, *Science*, *258*, 640–643.
- Harmon, J. K., M. A. Slade, and M. S. Rice (2011), Radar imagery of Mercury's putative polar ice: 1999–2005 Arecibo results, *Icarus*, *211*, 37–50.
- Hayne, P. O., B. T. Greenhagen, M. C. Foote, M. A. Siegler, A. R. Vasavada, and D. A. Paige (2010), Diviner lunar radiometer observations of the LCROSS impact, *Science*, *330*, 477–479, doi:10.1126/science.1197135.
- Hayne, P. O., O. Aharonson, J. L. Bandfield, B. T. Greenhagen, and D. A. Paige (2012), The surface roughness of the Moon from Diviner infrared observations, Abstract 2829 presented at 43rd Lunar and Planetary Science Conference, held March 19–23, 2012 at The Woodlands, Tex.
- Helfenstein, P., and M. K. Shepard (1999), Submillimeter-scale topography of the lunar regolith, *Icarus*, *141*, 107–131.
- Ingersoll, A. P., T. Svitek, and B. C. Murray (1992), Stability of polar frosts in spherical bowl-shaped craters on the Moon, Mercury, and Mars, *Icarus*, *100*, 40–47.
- Keihm, S. J., K. Peters, M. G. Langseth, and J. L. Chute (1973), Apollo 15 measurement of lunar surface brightness temperatures: Thermal conductivity of the upper 1-1/2 meters of regolith, *Earth Planet. Sci. Lett.*, *19*, 337–351.
- Kopp, G., and J. L. Lean (2011), A new, lower value of total solar irradiance: Evidence and climate significance, *Geophys. Res. Lett.*, *38*, L01706, doi:10.1029/2010GL045777.
- Küppers, M., et al. (2014), Localized sources of water vapour on the dwarf planet (1) Ceres, *Nature*, *505*(7484), 525–527.
- Ledlow, M. J., J. O. Burns, G. R. Gisler, J. Zhao, M. Zeilik, and D. N. Baker (1992), Subsurface emissions from Mercury: VLA radio observations at 2 and 6 centimeters, *Astrophys. J.*, *384*, 640–655.
- Li, J. Y., L. A. McFadden, J. W. Parker, E. F. Young, S. A. Stern, P. Thomas, C. T. Russell, and M. V. Sykes (2006), Photometric analysis of 1 Ceres and surface mapping from HST observations, *Icarus*, *182*(1), 143–160.
- Mazarico, E., G. A. Neumann, D. E. Smith, M. T. Zuber, and M. H. Torrence (2011), Illumination conditions of the lunar polar regions using LOLA topography, *Icarus*, *211*, 1066–1081, doi:10.1016/j.icarus.2010.10.030.
- McCord, T. B., J. Castillo-Rogez, and A. Rivkin (2011), Ceres: Its origin, evolution and structure and Dawn's potential contribution, *Space Sci. Rev.*, *163*, 63–76.
- Morrison, D. (1969), Thermal models and microwave temperatures of the planet Mercury, *Smithsonian Astrophys. Obs. Spec. Rep. No. 292*, Smithsonian Inst. Astrophys. Obs., Cambridge, Mass.
- Oberbeck, V. R. (1975), The role of ballistic erosion and sedimentation in lunar stratigraphy, *Rev. Geophys.*, *13*, 337–362.
- Paige, D. A., S. E. Wood, and A. R. Vasavada (1992), The thermal stability of water ice at the poles of Mercury, *Science*, *258*, 643–636.
- Paige, D. A., et al. (2009), The lunar reconnaissance orbiter diviner lunar radiometer experiment, *Space Sci. Rev.*, *150*, 125–160, doi:10.1007/s11214-009-9529-2.
- Paige, D. A., et al. (2010), Diviner lunar radiometer observations of cold traps in the Moon's south polar region, *Science*, *330*, 479–482.
- Pike, R. J. (1977), Apparent depth/apparent diameter relation for lunar craters, in *Proceedings of the 8th Lunar Planetary Science Conference*, pp. 3427–3436.
- Rambaux, N., J. Castillo-Rogez, V. Dehant, and P. Kuchynka (2011), Constraining Ceres' interior from its rotational motion, *Astron. Astrophys.*, *535*, A43, doi:10.1051/0004-6361/201116563.
- Rosenburg, M. A., O. Aharonson, J. W. Head, M. A. Kreslavsky, E. Mazarico, G. A. Neumann, D. E. Smith, M. H. Torrence, and M. T. Zuber (2011), Global surface slopes and roughness of the Moon from the Lunar Orbiter Laser Altimeter, *J. Geophys. Res.*, *116*, E02001, doi:10.1029/2010JE003716.
- Schorghofer, N. (2007), Theory of ground ice stability in sublimation environments, *Phys. Rev. E*, *75*, 041201, doi:10.1103/PhysRevE.75.041201.
- Schorghofer, N. (2008), The lifetime of ice on main belt asteroids, *Astrophys. J.*, *682*, 697–705.
- Schorghofer, N., and G. J. Taylor (2007), Subsurface migration of H<sub>2</sub>O at lunar cold traps, *J. Geophys. Res.*, *112*, E02010, doi:10.1029/2006JE002779.
- Spencer, J. R. (1990), A rough-surface thermophysical model for airless planets, *Icarus*, *83*, 27–38.
- Thomas, P. C., J. W. Parker, L. A. McFadden, C. T. Russell, S. A. Stern, M. V. Sykes, and E. F. Young (2005), Differentiation of the asteroid Ceres as revealed by its shape, *Nature*, *437*, 224–226, doi:10.1038/nature03938.
- Titus, T. N. (2015), Ceres: Predictions for near-surface water ice stability and implications for plume generating processes, *Geophys. Res. Lett.*, *42*, 2130–2136, doi:10.1002/2015GL063240.
- Tu, L., W. H. Ip, and Y. C. Wang (2014), A sublimation-driven exospheric model of Ceres, *Planet. Space Sci.*, *104*, 157–162.
- Vasavada, A. R., D. A. Paige, and S. E. Wood (1999), Near-surface temperatures on Mercury and the Moon and the stability of polar ice deposits, *Icarus*, *141*, 179–193.
- Vasavada, A. R., J. L. Bandfield, B. T. Greenhagen, P. O. Hayne, M. A. Siegler, J.-P. Williams, and D. A. Paige (2012), Lunar equatorial surface temperatures and regolith properties from the Diviner Lunar Radiometer Experiment, *J. Geophys. Res.*, *117*, E00H18, doi:10.1029/2011JE003987.
- Vincent, J. B., et al. (2014), Crater depth-to-diameter distribution and surface properties of (4) Vesta, *Planet. Space Sci.*, *103*, 57–65.
- Wasserburg, G. J., G. J. F. MacDonald, F. Hoyle, and W. A. Fowler (1964), Relative contributions of uranium, thorium, and potassium to heat production in the earth, *Science*, *143*, 465–467.
- Watson, K., B. C. Murray, and H. Brown (1961), The behavior of volatiles on the lunar surface, *J. Geophys. Res.*, *66*, 3033–3045, doi:10.1029/JZ066i009p03033.
- Whipple, F. L. (1950), A comet model. I. The acceleration of Comet Encke, *Astrophys. J.*, *111*, 375–394, doi:10.1086/145272.
- Zhang, J., and D. A. Paige (2009), Cold-trapped organic compounds at the poles of the Moon and Mercury: Implications for origins, *Geophys. Res. Lett.*, *36*, L16203, doi:10.1029/2009GL038614.
- Zuber, M. T., et al. (2000), The shape of 433 Eros from the NEAR-Shoemaker Laser Rangefinder, *Science*, *289*, 2097–2101, doi:10.1126/science.289.5487.2097.